Ion-specific hydrogel microcarriers with biomimetic niches for bioartifical liver system

Xiang Lin[1,2,3], Jinbo Li[1,2], Jinglin Wang [1,], Anne M. Filppula[3], Hongbo Zhang [3,4,]*, Yuanjin Zhao[1,2,]**

[1] Department of Rheumatology and Immunology, Nanjing Drum Tower Hospital, School of Biological Science and Medical Engineering, Southeast University, Nanjing 210096, China

[2] Oujiang Laboratory (Zhejiang Lab for Regenerative Medicine, Vision and Brain Health), Wenzhou Institute, University of Chinese Academy of Sciences, Wenzhou, Zhejiang 325001, China

[3]Pharmaceutical Sciences Laboratory, Åbo Akademi University, Turku, 20520, Finland

[4]Turku Bioscience Centre, University of Turku and Åbo Akademi University, Turku, 20520, Finland
Email: yjzhao@seu.edu.cn (Y.J.Zhao); hongbo.zhang@abo.fi (H.B.Zhang); cw20120817@163.com (J.L.Wang)

Keywords: microfluidics; hydrogel; silk protein; ice-template; acute liver failure

Bioartificial livers have showcased significant value in the treatment of acute liver failure (ALF). Current efforts are directed towards overcoming challenges in the development of microcarriers, with a specific emphasis on integrating higher-density liver cells to enhance detoxification capabilities. Here, inspired by the radial filtration model in hepatic lobules, we propose ion-specific silk fibroin microcarriers with biomimetic niches for cultivating functional liver cells at high density. These biomimetic microcarriers were generated by capillary microfluidic device with controllable adjustments of ion type or concentration within the aqueous phase. When cultivating human induced pluripotent stem cell (hiPSC)-differentiated mature liver cells on these recrystallized microcarriers, we observed notably enhanced cell proliferation activity, as well as increased metabolic and secretory functionality. Based on these features, we demonstrate that the microcarrier-integrated bioreactors could effectively reduce hepatic transaminase levels and significantly improve urea, albumin production and survival rate in rabbit ALF models. Thus, we believe that the biomimetic microcarriers and their derived bioreactors may hold potential for clinical applications in managing ALF and other liver

diseases.

1. Introduction

Liver damage and eventual failure can result from various factors, including viral infections, alcohol abuse, obesity, and genetic predisposition. [1] Although liver transplantation remains a life-saving treatment for end-stage liver disease, its practicality is still limited due to organ shortages and the necessity for long-term immunosuppressive therapy. [2] The emerging bioartificial liver (BAL) system, which mimics liver functions and sustains essential patient activities *in vitro*, offers a promising alternative to transplantation. [3] However, achieving high-density liver cell culture in BAL systems poses challenges as simply culturing cells on the surface of microcarriers does not actually increase cell density. [4] Although many commercially available biomaterials could provide high surface area scaffolds for cell culture, most of them come with inherent biotoxicity due to intricate synthesis processes. [5]Moreover, liver cells, being highly polarized, require specific environmental cues within three-dimensional niches to perform functions like glycogen storage, cytochrome P450 (CYP) family proteins production. [6] Hence, it is imperative to devise new biological materials that promote the growth of liver cells to establish a highly efficient integrated BAL system.

Here, inspired by the radial filtration model observed in hepatic microstructural units, we propose a novel ion-specific silk fibroin microcarrier with biomimetic niches for acute liver failure (ALF), as illustrated in **Figure 1**. The utility of degummed silk fibroin is underscored by its minimal susceptibility to immune rejection, aligning well with the stringent criteria mandated by the US Food and Drug Administration in terms of biomaterials. [7] With the assistance of microfluidic technology, which can precisely control different phases of fluid, the natural silk fibroin could be tailored into different morphology particles. [8] Ice recrystallization is a common natural phenomenon. For example, the recrystallization of sea ice produces prebiotic substances. [9] By utilizing the hoffmeister effect, the ice recrystallization process can be conveniently and effectively controlled, which is conducive to promoting the generation of large ice crystals and creating space for life development. [10] Therefore, by combining silk fibroin with the hoffmeister effect through microfluidic technology, we have the potential to prepare in vitro biomimetic liver models with high liver cell density microcarriers.

To realize this concept, we generated a large number of silk fibroin microcarriers using a capillary microfluidic device. By altering the type or concentration of ions in the aqueous phase

solution during the initial stage, the niches size after recrystallization can be adjusted within tens of microns. Considering potential risks such as immunogenic responses to porcine hepatocytes and zoonosis diseases, human induced pluripotent stem cell (hiPSC)-differentiated mature liver cells were selected as the basic functional unit of the biomimetic liver lobules. *In vitro* cultures of the recrystallized microcarriers revealed enhanced proliferation activity, as well as heightened metabolic and secretory functionality. Based on this, we conducted an animal experiment utilizing the microcarriers-integrated bioreactor to address ALF in rabbit models. The outcomes underscored a substantial reduction in hepatic transaminase levels and significant improvements in animal survival rate. These results indicated that our biomimetic bioartifical liver system has great potential in the treatment of ALF, opening exciting avenues for potential clinical applications.

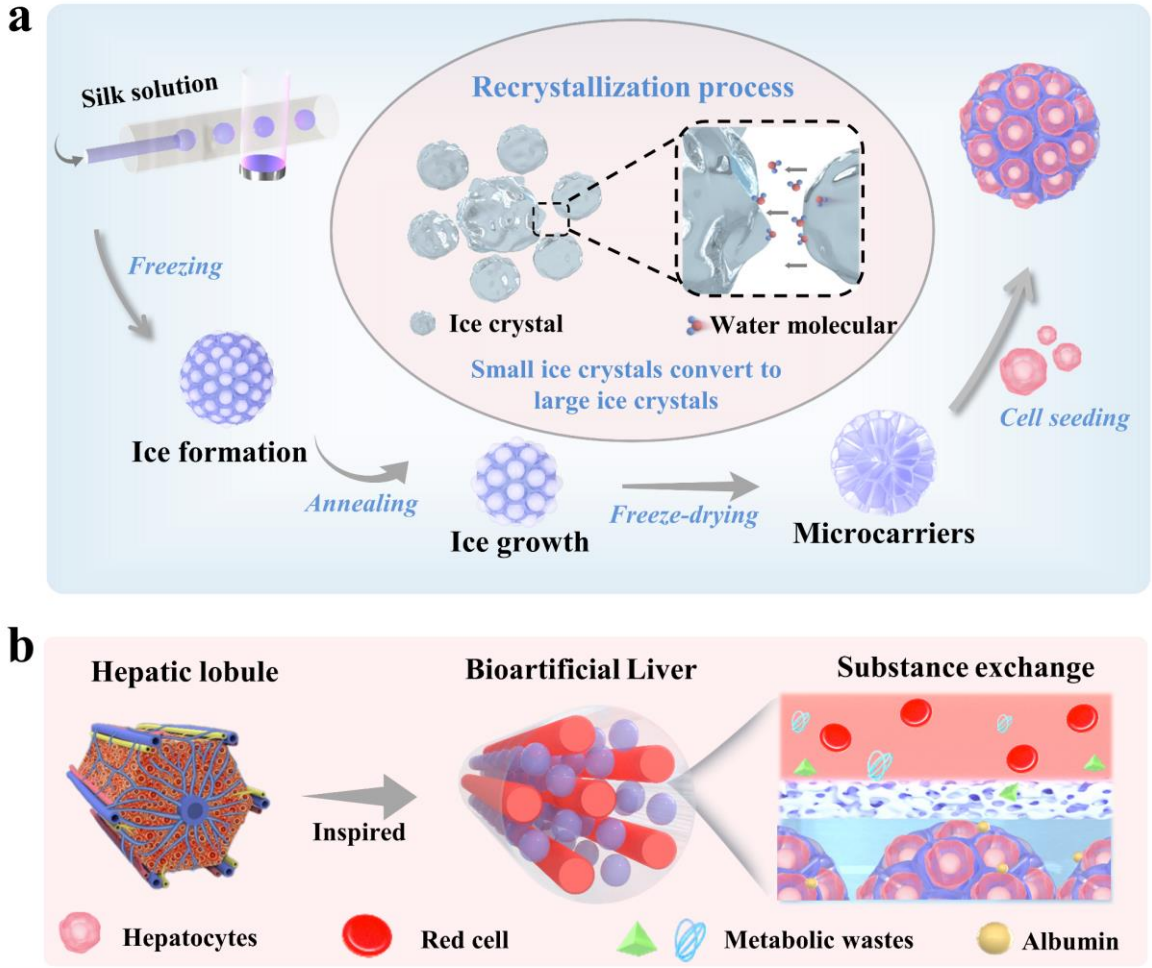

Figure 1. (a) Schematic of ion-specific control of recrystallization in microcarriers and cell seeding process, (b) Illustration of the bioreactor combined with hepatocytes microcarriers for the treatment of ALF.

2.Results and Discussion

In a typical example, we combined microcarriers and semipermeable microtubules to construct a radial hepatic lobular bioreactor (**Figure 2**). The hepatic lobules exhibit an approximately hexagonal shape, featuring diameters ranging from 1 to 2 millimeters (**Figure 2a**). Hepatocytes are arranged in a radial pattern along the central vein within these lobules. The purified blood, carrying these filtered substances, is then transported by the central vein into larger blood vessels within the liver (**Figure 2b-d**). Silk fibroin microcarriers designed to replicate hepatic cell growth environment were synthesized via microfluidics (**Figure 2e**). In the presence of UV light and ruthenium (Ru)/sodium persulfate (SPS), covalent dityrosine bonds were established between tyrosine residues (**Figure S1a**). Silk fibroin boasts a tyrosine content, which affords the opportunity to achieve cross-linked silk fibroin microcarriers without subjecting biological materials to complex chemical treatments. The photopolymerization time of silk fibroin solutions with 3% and higher concentrations is less than three seconds (**Figure S1b**). To ensure the mechanical properties of resultant hydrogel can align with further application, a 5% solution of silk fibroin was chosen for the microcarriers fabrication process.

The microcarrier's size was tunable by altering the flow rate between the two solution phases (**Figure 2f**). Increasing the internal water phase flow rate enlarged the microcarrier diameter, while decreasing the external oil phase flow rate had a similar effect (**Figure S2**). In addition, the generated microcarriers exhibited a consistent morphology and a high level of monodispersity (**Figure 2g&S3**). To evaluate their biocompatibility, cells were co-cultured with washed microcarriers, there was no significant impact on their proliferation or morphology, and their proliferation rate remained the same with the control group (**Figure S4**). This favorable outcome can be attributed to the facile removal of the water-soluble photoinitiator during the washing process. The radial structure can be simulated by an *in vitro* bioreactor, and the liver cells in the constructed bioreactor can filter metabolic waste in the body (**Figure 2h**). The semipermeable microtubes, which simulate the central vein of the hepatic lobule, had micropores on their surfaces for substance exchange with the surrounding liver cells. The former generated microcarriers can be submerged in the necessary cell culture medium and can be conveniently integrated to form a biomimetic bioreactor (**Figure 2i-j**).

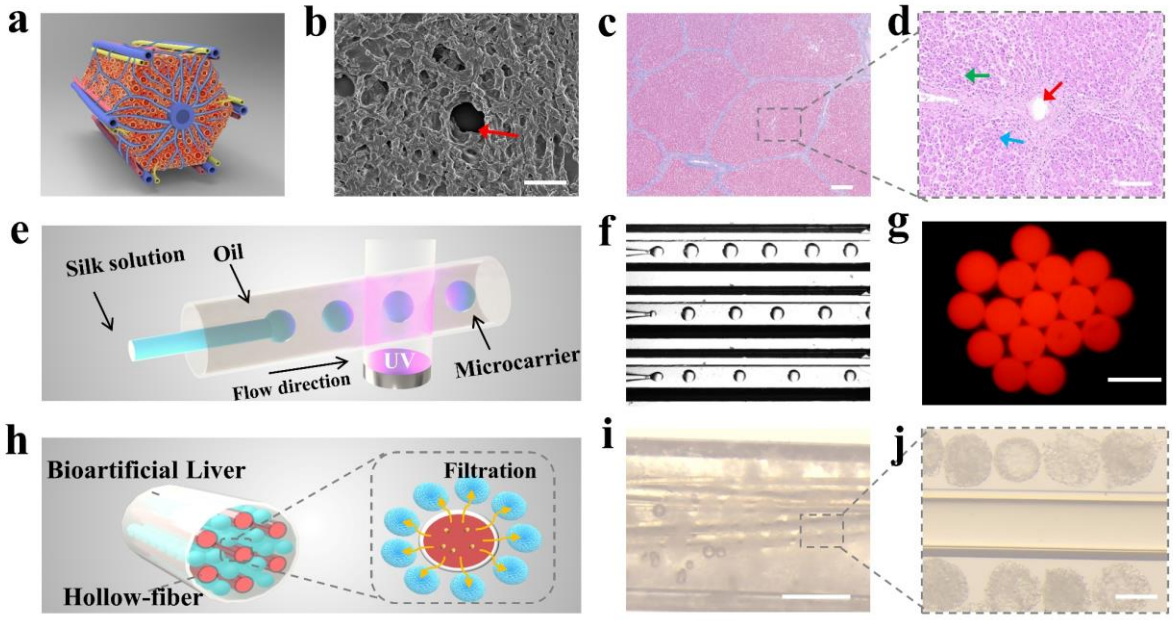

Figure 2 The process of preparing BAL model in vitro, a) The hexagonal lobular structure of the liver, b) Scanning electron microscopy (SEM) image of the corresponding frozen-drying liver section, c) Masson staining photos of liver tissue, d) The liver microstructure stained by H&E, the blue arrow represents the liver parenchymal cells, the red arrow represents the central vein, the green arrow represents the liver blood sinus, e) Crosslinking schematic diagram of silk fibroin hydrogel microcarrier, f) Generation process of microcarriers in a microfluidic device at different flow rates, the inner/outer flow rates ratio were 0.15/1, 0.15/1.5, 0.1/1.5 mL h^{-1}, respectively, g) Silk fibroin microcarriers stained with Rhodamine B, h) A schematic diagram of bioartificial liver, i) Distribution of multiple microtubules within the bioreactor, j) Arrangement of microcarriers around the semi-permeable tube. The scale bar is 50 μm in b), 200 μm in c), 50 μm in d), 400 μm in g) and 500 μm in i), 200 μm in j).

Controlling the formation of ice crystals is crucial for the controllable preparation of porous materials. Ice recrystallization process influenced by specific ions, offers adjustable control on ice crystal size and serves as a template for creating pores within microcarriers. Using the "splat-cooling" method, we assessed the ability of three different ions (F^-、Br^-、I^-) in regulating ice crystal formation in a 2 % silk fibroin solution (**Figure 3a&c**). Recrystallization mainly follows the Ostwald ripening process. The ice crystals can grow at the expense of smaller crystals, increasing average crystal size and reducing total crystal count (**Figure 3b**). Ice crystals obtained from a NaI solution had an average size of 105.6 ± 6.5 μm, while NaF group had significantly reduced ice crystal size compared to the pure water group (78.6 ± 7.1 μm) (**Figure**

3d). The mean recrystallized pore size of the NaBr group was similar to the pure water group after annealing for 60 minutes (**Figure S5a**). Similar phenomena were also observed in the three-dimensional matrix of silk fibroin solution (**Figure S6**). Therefore, it is possible to adjust the average size of ice crystals by changing the type of anions in the silk protein solution.

Furthermore, we conducted the assessment of the impact of various anions on ice recrystallization. Compared to pure water, both SO_4^{2-} and HPO_4^{2-} exhibited stronger inhibitory effects on ice recrystallization, whereas ice particles formed in the presence of NO_3^-, and I^- were considerably larger (**Figure S7a**). Furthermore, when considering the effect of cations on pore size, we note that cations have a less significant effect on ice recrystallization than anions. Compared with pure water, Mg^{2+} and Li^+ have inhibitory effects on ice crystal growth, and the pores formed in the presence of K^+ are larger than those formed in pure water. (**Figure S7b**).

The recrystallization process can be determined through quenching and annealing. The quenching parameter can adjust the nucleation, while annealing can adjust ice growth. To gain deeper insights into the factors influencing the recrystallization process, we investigated the effects of quenching and annealing on ice crystal size. As the quenching temperature increased, the effect of quenching temperature on the average grain size was minimal (**Figure S8a**). However, the change of temperature during the annealing process influenced the ice crystal size (**Figure S8b**). Since the quenching temperature has little effect on the ice crystal size, the nucleation process has a small impact on the average ice crystal. In contrast, the annealing temperature plays a significant role in determining the average crystal size at a certain ion concentration. Besides, the size of recrystallized ice crystals followed the same order in different salt concentrations (**Figure S8c**). Among the 5% silk fibroin microcarriers, those containing NaI displayed the largest pore structures (**Figure 3e and S5b**).

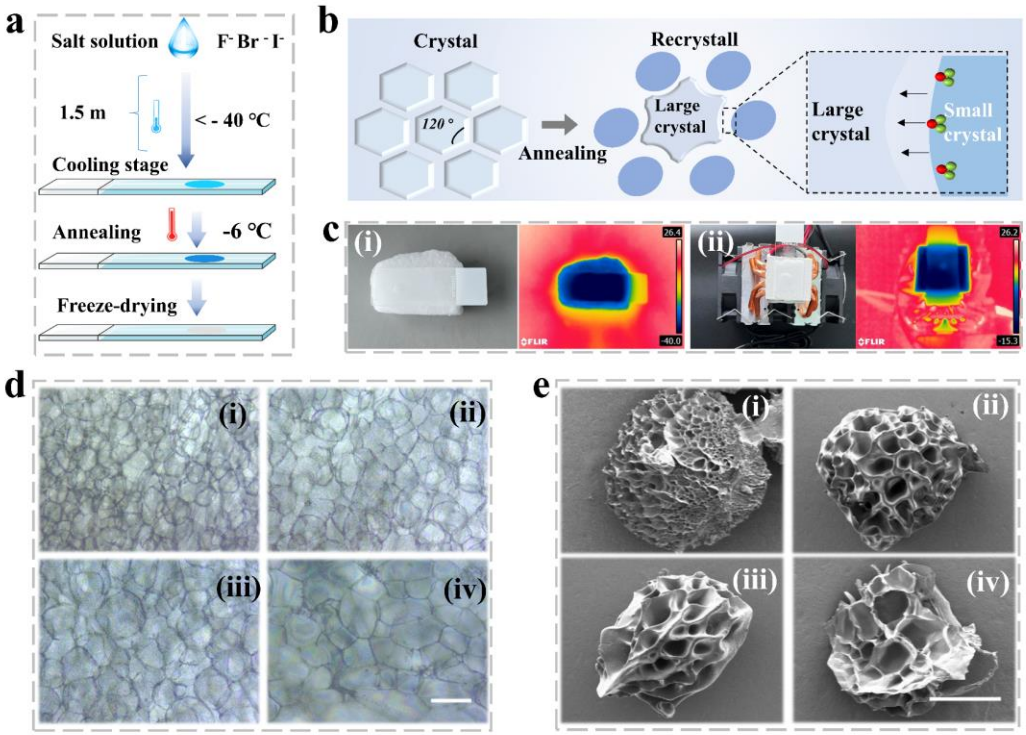

Figure 3. a) Schematic image of the "splat-cooling" process, b) The ice recrystallization process, c) i) Quenching process with corresponding infrared thermal images, ii) Annealing process with corresponding infrared thermal image, d) Images of various ions and pure water on the recrystallization of 2% silk fibroin with different groups: (i) F^- group, (ii) pure water group, (iii) Br^- group, (iv) I^- group. e) SEM images of microcarriers after different ion regulated recrystallization, (i) F^- group, (ii) pure water group, (iii) Br^- group, (iv) I^- group. The scale bar is 80 μm in d), 100 μm in e).

Given the immunogenicity of pig liver cells and the limitations of cancer cells in clinical applications, the hiPSCs were chosen as the basic functional unit of the liver lobule (**Figure 4**). A previously optimized induction protocol was employed to generate mature hepatocytes (Mhps) (**Figure 4a)**. Initially, hiPSCs were induced into hepatic progenitor cells, which were further matured after one week of induction to form mature hepatocytes. These induced cells were capable of normal expression of cytochrome P450 (CYP) family proteins such as CYP1A2 and CYP3A4 **(Figure 4b**). Additionally, the levels of expression factors were higher in microcarriers group compared to two-dimensional culture (**Figure 4f**). 80.9% of hiPSC-derived Mhps exhibited positive ALB (ALB^+) expression and negative alpha-fetoprotein (AFP) expression (AFP^-) **(Figure 4d-e**), and they also showed the secretion function of liver cells (**Figure S9**). It is worth noting that the marker AFP of liver progenitor cells further decreases with the increase of induction days (**Figure S10**). After three weeks of cultivation, Mhps cells

did not express AFP but expressed ALB secretion protein normally (**Figure S11**), these results indicated the successful induced of hiPSCs to Mhps.

Calcein staining revealed that Mhps cells, labeled with red fluorescence, exhibited sparse growth on the surface of microcarriers controlled by NaF. In contrast, the cells grown on the surface of NaI microcarriers after recrystallization maintain high cell density (**Figure 4c**). Furthermore, the corresponding Cell Counting Kit-8 (CCK8) cell activity results showed that the surface of the recrystallized microcarrier was able to adhere more cells and had good cell proliferation characteristics (**Figure S12**). Mhps in the microcarrier niches of on NaI groups were able to synthesize glycogen normally, with glycogen evenly distributed throughout the entire cell and producing more liver glycogen than petri dish cultures (**Figure S13**). The eliminate rate of Indocyanine Green (ICG) reflects the excretion function of the liver. The clearance rate of Mhps cultured on the surface of microcarriers was higher than that of cells cultured on two-dimensional plates (**Figure S14**). These results indicate that Mhps can growth well on recrystallized microcarriers and maintain liver specific function *in vitro*.

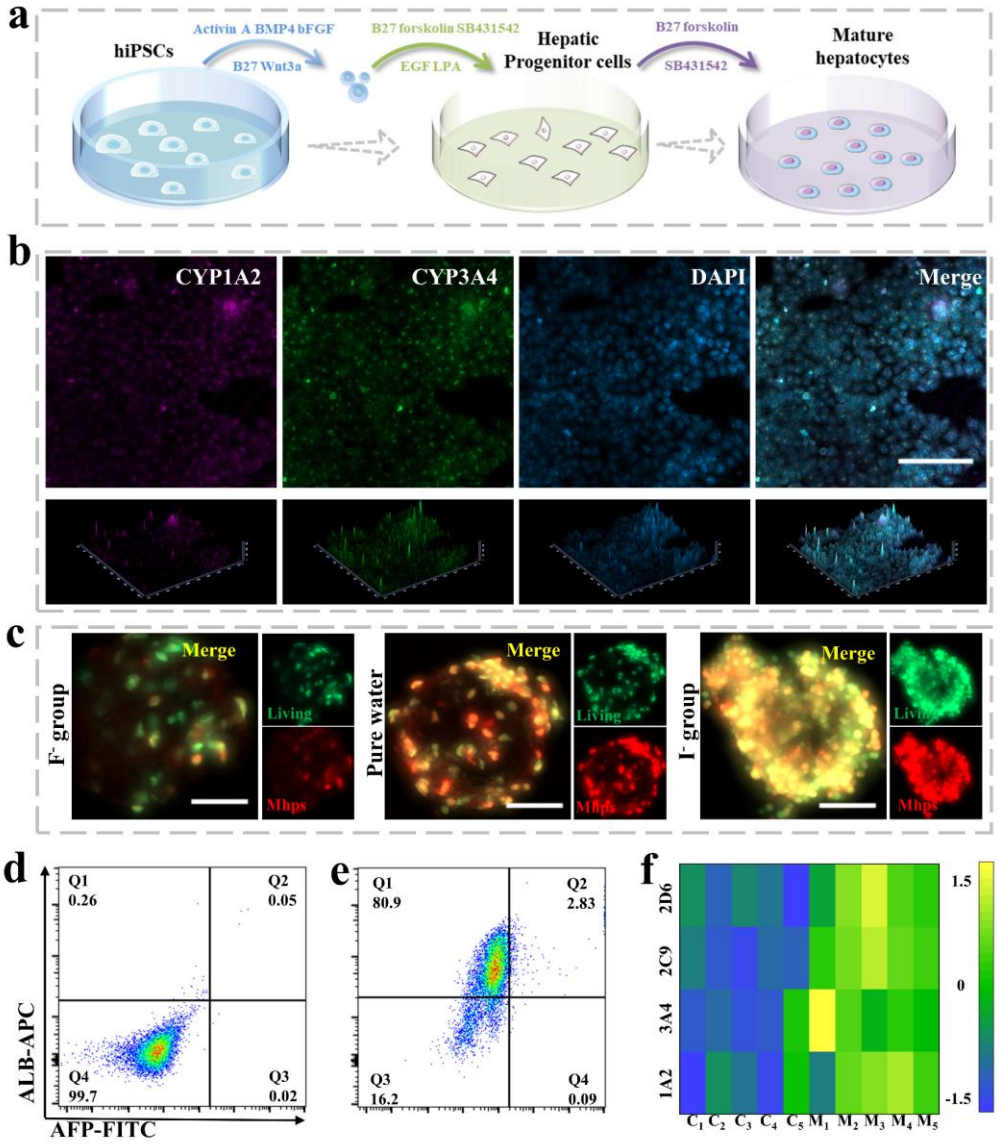

Figure 4 a) The process of inducing hiPSCs into Mhps, b) Immunofluorescence staining of CYP1A2 and CYP3A4 proteins in liver mature cells, c) Construction of pluripotent stem cells derived Mhps on different microcarriers, i) F^- group, (ii) pure water group, (iii) I^- group. d-e) Expression of AFP and ALB proteins in Mhps d) negative control and e) experiment group, f) The RT-qPCR tests of relative P-450 expression amounts in petri dish (C_1-C_5) and microcarriers (M_1-M_5). The scale bar is 100 μm in b) and c).

Although many types of bioreactors have been used clinically, the traditional two-dimensional cell culture models are limited for the exchange of oxygen and nutrients. Thus, we combined the recrystallized microcarriers with semipermeable microtubes to prepare a high-throughput bioreactor **(Figure 5)**. The BAL system consists of three loops. The separator separated blood and plasma to form the first loop. The second loop performed material exchange units between the bioreactor and plasma. The last loop is the nutrient supply cycle

established by the culture medium and bioreactor (**Figure 5a**). Rabbits were induced into ALF model through D-galactosamine (D-Gal), and the experiment groups were treated with the BAL system for four hours (**Figure 5b**). After treatment, the survival rate of rabbits with ALF significantly increased from 33 % to 68 % (**Figure 5d**), indicating that the liver had regained most of its original detoxification function, and the bioreactor was proven to be effective. Approximately 3×10^9 cells were encapsulated into the bioreactor, and ammonia consumption on the microcarriers in different groups was selected as an indicator of xenobiotic metabolism. Due to the large number of semipermeable microtubules and frequent material exchange, the ammonia elimination level and glucose consumption in the bioreactor are higher than those in the two-dimensional culture plate (**Figure 5e&f**). These results showed that the plasma flowing through the semipermeable tube can effectively exchange nutrients secreted in the liver culture unit while providing a certain liver detoxification function.

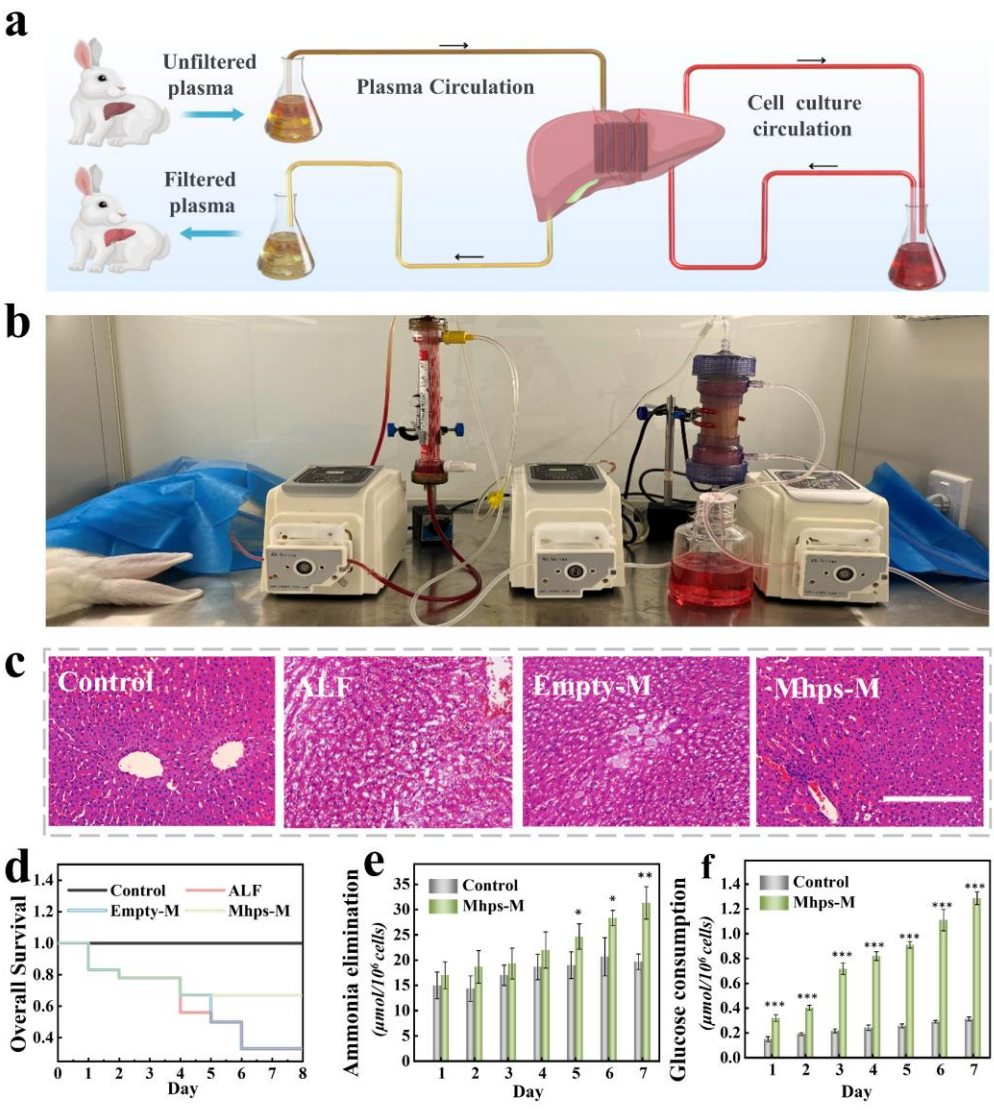

Figure 5. a) Diagram of the BAL system construction, b) Images of treatment for ALF in rabbits, c) H&E staining of different groups of ALF model; the control group was set as negative control, the ALF group was positive control, the Empty-M were treated with cell-free microcarrier based bioreactor, the Mhps-M were treated with Mhps-loading microcarrier based bioreactor, d) Statistic of overall survival rate in different groups (n = 6), e) Statistic of the ammonia elimination amount in different groups (n = 5), f) Statistic of the glucose consumption amount in different groups (n = 5). The scale bar is 100 μm in c). Data are presented as mean ± standard deviation. NS = no significant $*P < 0.05$, $**P < 0.01$, $***P < 0.001$.

Further analysis of ALF necrosis revealed that, compared to the untreated ALF group, the Mhps-M group showed a reduction in the proportion of liver cell necrosis (**Figure 5c&S15a**), as well as a significant decrease in cell apoptosis (**Figure 6a, e**). Ki67 staining showed that liver cells obtained a good regenerative capacity after treatment with the BAL. Notably, empty bioreactors without cell exchange did not exhibit therapeutic functionality (**Figure 6b, f**). Liver transaminase indicators showed a significant decrease (**Figure 6c-d**), and the urea synthesis and ALB secretion capabilities of treatment group were significantly improved (**Figure S15 b-c**). Therefore, the recrystallized microcarrier-integrated bioreactor significantly enhances the recovery of liver function in liver failure model, promoting the exchange of soluble factors and the elimination process of metabolic waste. These results demonstrate the effectiveness of the bioreactor in the treatment of ALF, highlighting its substantial potential in clinical therapy.

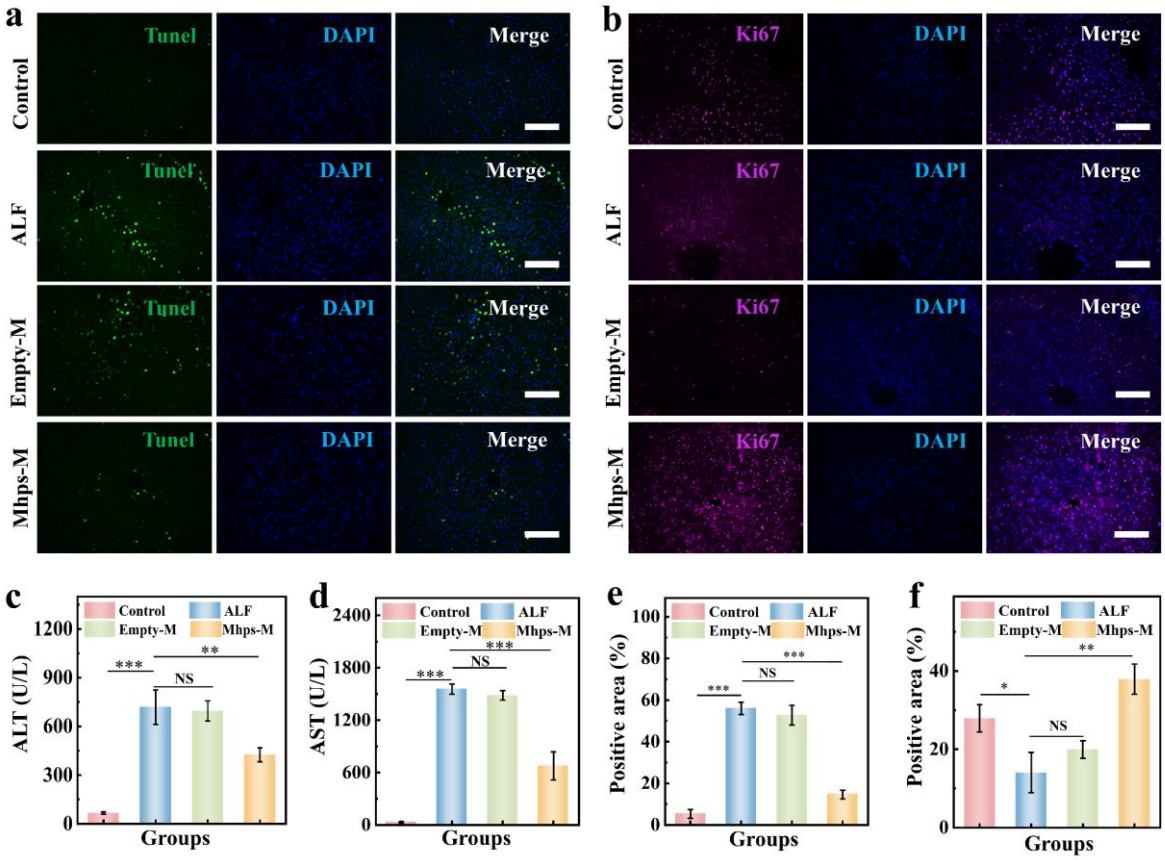

Figure 6 a) Immunofluorescence staining results of Tunel in different groups, b) Immunofluorescence staining results of Ki67 in different groups, c) Statistical data for liver function indicator ALT (n = 3), d) Statistical data for liver function indicator AST (n = 3), e) The corresponding statistic of Tunel positive area in four groups (n = 5), f) The corresponding statistic of Ki67 positive area in four groups (n = 5). The scale bar is 100 μm in a), b). Data are presented as mean ± standard deviation. NS = no significant, **P* < 0.05, ***P* < 0.01, ****P* < 0.001.

3.Conclusion

Here, we proposed a novel BAL system for treating acute liver failure. The preparation of hydrogels with biomimetic niches was controlled by the hoffmeister effect. Further, microcarriers with continuous, uniform, and high porosity were generated using microfluidic technology. After successfully inducing hiPSCs into mature liver cells, these cells were capable of growth within the biomimetic ecological niche pores on the microcarriers, exhibiting normal secretion and expression of detoxification-related cytokines. In animal experiments, the microcarriers were effectively integrated with a semi-permeable microtube to form a hollow fiber bioreactor and improved the animal survival rate. Future research directions for integrating

high-density cells into bioartificial bioreactors will continue to focus on portability, cost-effectiveness, suitability for clinical settings, and broader applications. Current bioreactors still have relatively large volumes, resulting in high costs and inconvenience in usage. Researchers will continue to refine bioreactor designs, employing advanced biomaterials and cell engineering techniques to enhance cell stability and function. The goal is to lower the barriers to using BAL systems, enabling more medical institutions and patients to benefit from this technology.

Methods

Materials: Silk fibroin was purchased from Suzhou Simete Biotechnology Co., Ltd. All salts were purchased from Aladdin Chemistry (America), and ultrapure water for experiments was prepared using Milli-Q. Rhodamine B was supplied by Hefei QiSheng Technology (China), H&E and Masson's reagents were provided by Servicebio (China). Ruthenium (Ru), sodium persulfate (SPS), calcium green, ICG powder were all purchased from Sigma (America). The PAS assay kit was acquired from Shanghai Shangbao Biotechnology (China).

Microcarrier Generation: Microcarriers were generated using a microfluidic device consisting of capillaries [11]. Microcarriers were formed through the shear action between water and oil phases. In brief, the inner phase consisted of 5% silk fibroin solution containing Ru/SPS. Silicon oil was used as the outer continuous phase. A coaxial capillary with an inner diameter of 580 micrometers was employed to create the microfluidic device. Droplets were sheared into circular microcarriers at the tip of the inner phase and, after generation in the oil phase, excess oil droplets were removed through ethanol and water washing. For create ion-specific microcarriers, we mixed the microcarrier with different ion solutions to perform recrystallization. For biocompatibility, 5 mg microcarriers generated with Ru/SPS at different molar mass ratios were co-cultured with Mhps for three days. And then tested with Calcein staining and CCK8-kit.

Recrystallization of hydrogel: Recrystallization of hydrogels was performed using the splate-cooling method. [9b] Silk fibroin solution (2 %) containing various ions was dropped onto glass slides on dry ice to rapidly forming ice crystals, followed by annealing at different temperatures based on experimental conditions. Subsequently, the pores created by freeze-drying process were documented using a metallographic microscope, with five data points recorded from three random fields in each group. 5 % Silk fibroin solution droplets were employed to test the ion recrystallization in three-dimensional hydrogels.

Tyrosine Quantification: For the cross-linked silk fibroin solution, the amount of tyrosine generated varied with different initiators and prepolymer concentrations. [12]The required pre-gel solution was mixed with Ru/SPS at different molar mass ratios (0.25/2.5, 0.5/5, 1/10 mM), and polymerized under UV light for 10 s. After polymerization, the hydrogel was placed under a UV light emitting at 302 nm, and images were captured with a camera. The images were then converted to grayscale values, and fluorescence intensity was quantified. Five mg microcarriers generated with Ru/SPS at different molar mass ratios were co-cultured with Mhps for three days.

Pluripotent stem cells induction into mature liver cells: hiPSCs were provided by the Affiliated Drum Tower Hospital of Nanjing University. The induction protocol followed previous descriptions. [2f] In brief, hiPSCs were cultured in a specialized induction medium for one day. The basal medium used was RPMI 1640, supplemented with Activin A (100 μg per liter), BMP4 (5 μg per liter), bFGF (10 μg per liter), Wnt3a (20 μg per liter), and 1% B27. Subsequently, they were transferred to a culture medium without Wnt3a and B27 for an additional 3 days, leading to the formation of endoderm cells. The endoderm cells were further cultured in a medium containing KGF (20 μg per liter), SB431542 (5×10^{-6}M), and 1% B27 for 2 days. Afterward, they were transferred again to a medium containing KGF (20 μg per liter), BMP4 (20 μg per liter), BMP2 (10 μg per liter), bFGF (10 μg per liter), and B27(1%) for 3 days, forming hepatoblasts. To generate hepatic progenitor cells, the hepatoblasts were induced in DMEM/F12 medium for 7 days, supplemented with B27(1%), SB421542 (5×10^{-6} M), EGF (20 μg per liter), CHIR99021 (3×10^{-6} M), LPA (5×10^{-6} M), dexamethasone (1×10^{-6} M), and S1P (5×10^{-7} M). For further induction into mature liver cells, hepatic progenitor cells were seeded in Williams' E medium (with B27, thyroid hormone, and SB431542) for three weeks.

Cell Culture on Microcarriers: After recrystallization and freeze-drying, the microcarriers were sterilized overnight under ultraviolet light. Cell viability was observed through Calcein-AM staining. For CCK8 proliferation assays, an equal number of cells were seeded on microcarriers, with 1 mg of freeze-dried microcarriers of different groups. 10 % staining reagents were added to the culture medium, and OD values were recorded. For real-time fluorescent PCR: Primer design was provided by Zhejiang Shangya Company. The total RNA was extracted from cells grown on the surface of microcarriers using an RNA extraction kit, and it was further reverse-transcribed into cDNA for further analysis, with each experiment repeated three times.

Liver Cell Functional Assessment: Immunofluorescence staining for ALB (Proteintech), AFP (Abcam), CYP1A2, and CYP3A4 (Absin) was performed using standard staining techniques. The secretion level of ALB as well as AFP in Mhps was measured by flow cytometry. For PAS staining, cell slides were oxidized with an oxidizing agent for 5-10 minutes, followed by staining with Schiff Reagent for 10-15 minutes. ICG powder was purchased from Aladdin. In summary, cells were seeded on well plates and microcarriers, and then ICG powder was added to the culture medium to form a 1 mg/mL staining solution. After 15 minutes, the cells were washed three times, new culture medium for normal culture was added. The clearance rate of different groups at different time points was recorded.

Determination of Bioreactor Detoxification Capability: Ammonia concentration was defined to assess the initial detoxification function of liver cells. Ammonia concentration measurements were performed using a blood ammonia concentration determination kit (Abcam). Briefly, dispense a total of 100 μL of sample per well in a 96-well plate. Add 80 μL of Reagent II/Reagent 1 to each standard and sample well. Follow this by adding 40 μL of Reagent III/Reagent 2 to each well. Incubate the plate at 37°C for 30 minutes. After incubation, measure the optical density (OD) at 670 nm using a microplate reader. Glucose consumption was determined using a colorimetric-based glucose content assay kit (Solarbio).

Animal Experiment: Approximately two months old New Zealand white rabbits were used in an ALF model experiment. The experiment was divided into negative control group (six animals each group), acute liver failure group, cell-free treatment group (Empty-M), and bioreactor treatment group (Mhps-M). ALF was induced by injecting D-Gal at a dose of 0.6 g per kilogram. One day after induction, all experimental rabbits were used for the experiment. The whole blood was separated using a blood plasma separator, and at a flow rate of 25 mL per minute, plasma was introduced into the bioreactor at a rate of 5 mg/mL to create a second circulation, with waste exchanged with the cell culture medium inside the reactor to simulate liver metabolism processes. The entire process lasted for four hours, and ethical approval for animal research was granted by Laboratory Animal Center of WIUCAS (No. WIUCAS23072605).

Immunohistochemical Staining: Rabbits that were alive on the third day after experiment were euthanized using high-concentration carbon dioxide. Liver tissues were fixed in paraformaldehyde. After fixation, the tissues underwent dehydration, paraffin embedding, and staining with hematoxylin and eosin before being sealed with coverslips for photography. The area of necrosis was recorded and quantified. Ki67 staining was used to assess cell proliferation,

while Tunel staining was used to evaluate apoptosis. Five randomly selected fields measuring 1 mm^2 each were used to calculate the ratio of positive cells.

Statistical Analysis: We utilized an independent sample t-test to examine the statistical significance between the two compared groups. The "$p < 0.05$" were selected as significance level, and "*" indicating "$0.01 < p < 0.05$", "**" means "$p < 0.01$", *** means "$p < 0.001$" The processed data were presented as mean values with their corresponding standard deviations.

Supporting Information

Supporting Information is available from the Wiley Online Library or from the author.

Acknowledgements

This work was supported by the National Key Research and Development Program of China (2022YFA1105300), the National Natural Science Foundation of China (52073060), the Guangdong Basic and Applied Basic Research Foundation (2021B1515120054), the Nanjing Medical Science and Technique Development Foundation (ZKX21019), the Clinical Trials from Nanjing Drum Tower Hospital (2022-LCYJ-ZD-01), the Research Fellow (Grant No.353146), Project (347897), Solution for Health Profile (336355), InFLAMES Flagship (337531) grants from Research Council of Finland, and Finland China Food and Health International Pilot Project funded by the Finnish Ministry of Education and Culture.

Author contributions

Y.J.Z. conceived the idea and designed the experiment; X.L. conducted experiments and data analysis; J.L.W and J.B.L assisted with cell culture; X.L., A. F., H.B. Z and Y.J.Z. wrote the manuscript. Y.J.Z supervised the manuscript.

References

[1] a)J. Gracia-Sancho, E. Caparrós, A. Fernandez-Iglesias, R. Frances, *Nature Reviews Gastroenterology & Hepatology* **2021**, 18, 411; b)L. Hammerich, F. Tacke, *Nature Reviews Gastroenterology & Hepatology* **2023**, 20, 633; c)T. Li, X. Fan, M. Cai, Y. Jiang, Y. Wang, P. He, J. Ni, A. Mo, C. Peng, J. Liu, *Science of The Total Environment* **2023**, 167167.

[2] a)P. Burra, C. Becchetti, G. Germani, *JHEP reports* **2020**, 2, 100192; b)J. Colmenero,

M. Rodríguez-Perálvarez, M. Salcedo, A. Arias-Milla, A. Muñoz-Serrano, J. Graus, J. Nuño, M. Gastaca, J. Bustamante-Schneider, A. Cachero, *Journal of hepatology* **2021**, 74, 148; c)F. Durand, J. Levitsky, F. Cauchy, H. Gilgenkrantz, O. Soubrane, C. Francoz, *Journal of Hepatology* **2019**, 70, 745; d)H. Tilg, T. E. Adolph, M. Dudek, P. Knolle, *Nature metabolism* **2021**, 3, 1596; e)R. van Rijn, I. J. Schurink, Y. de Vries, A. P. van den Berg, M. Cortes Cerisuelo, S. Darwish Murad, J. I. Erdmann, N. Gilbo, R. J. de Haas, N. Heaton, *New England Journal of Medicine* **2021**, 384, 1391; f)J. Wang, H. Ren, Y. Liu, L. Sun, Z. Zhang, Y. Zhao, X. Shi, *Advanced Healthcare Materials* **2021**, 10, 2101580.

[3] a)S. Chen, J. Wang, H. Ren, Y. Liu, C. Xiang, C. Li, S. Lu, Y. Shi, H. Deng, X. Shi, *Cell research* **2020**, 30, 95; b)J. Guan, G. Wang, J. Wang, Z. Zhang, Y. Fu, L. Cheng, G. Meng, Y. Lyu, J. Zhu, Y. Li, *Nature* **2022**, 605, 325; c)J. Lou, D. J. Mooney, *Nature Reviews Chemistry* **2022**, 6, 726.

[4] a)R. Curvello, V. Kast, P. Ordóñez-Morán, A. Mata, D. Loessner, *Nature Reviews Materials* **2023**, 1; b)R. M. Rumney, S. C. Robson, A. P. Kao, E. Barbu, L. Bozycki, J. R. Smith, S. M. Cragg, F. Couceiro, R. Parwani, G. Tozzi, *Nature Communications* **2022**, 13, 3753.

[5] a)K. Debnath, K. Las Heras, A. Rivera, S. Lenzini, J.-W. Shin, *Nature Reviews Materials* **2023**, 8, 390; b)X. Ding, Y. Yu, L. Shang, Y. Zhao, *ACS nano* **2022**, 16, 19533; c)H. Gao, S. Q. Wang, Z. H. Liu, J. T. Hirvonen, H. A. Santos, *Acs Applied Bio Materials* **2023**, 6, 4269; d)L. Yang, Y. Liu, L. Sun, C. Zhao, G. Chen, Y. Zhao, *Nano-Micro Letters* **2022**, 14, 1; e)X. D. Zhang, T. Wang, Z. Y. Zhang, H. Q. Liu, L. F. Li, A. C. Wang, J. Ouyang, T. Xie, L. Q. Zhang, J. J. Xue, W. Tao, *Materials Today* **2023**, 68, 177.

[6] a)A. Bashir, A. Duseja, A. De, M. Mehta, P. Tiwari, *Liver Research* **2022**, 6, 72; b)N.-S. Lau, M. Ly, K. Liu, A. Majumdar, G. McCaughan, M. Crawford, C. Pulitano, *Transplantation* **2022**, 106, 1339; c)S. Morales-Conde, E. Licardie, I. Alarcón, A. Balla, *Cirugía Española (English Edition)* **2022**, 100, 534; d)T. Yokomizo, T. Ideue, S. Morino-Koga, C. Y. Tham, T. Sato, N. Takeda, Y. Kubota, M. Kurokawa, N. Komatsu, M. Ogawa, *Nature* **2022**, 609, 779.

[7] a)C. Dai, D. Kong, C. Chen, Y. Liu, D. Wei, *Advanced Functional Materials* **2023**, 2301948; b)S. Ghalei, H. Handa, *Materials today chemistry* **2022**, 23, 100673; c)X. Yao, S. Zou, S. Fan, Q. Niu, Y. Zhang, *Materials Today Bio* **2022**, 100381; d)S. Zou, X. Yao, H. Shao, R. L. Reis, S. C. Kundu, Y. Zhang, *Acta Biomaterialia* **2022**.

[8] a)J. M. Ayuso, M. Virumbrales-Muñoz, J. M. Lang, D. J. Beebe, *Nature communications* **2022**, 13, 3086; b)Q. C. Li, Q. C. Song, W. Guo, Y. Cao, X. Y. Cui, D. R. Chen, H. C. Shum, *Angewandte Chemie-International Edition* **2023**; c)X. Lin, J. Wang, X. Wu, Y. Luo, Y. Wang, Y. Zhao, *Advanced Functional Materials* **2023**, 33, 2211323; d)L. Shang, F. Ye, M. Li, Y. Zhao, *Chemical Society Reviews* **2022**, 51, 4075; e)Q. Wang, C. Wang, X. Yang, J. Wang, Z. Zhang, L. Shang, *Smart Medicine* **2023**, 2, e20220027.

[9] a)M. Lin, H. Cao, J. Li, *Acta Biomaterialia* **2022**; b)S. Wu, C. Zhu, Z. He, H. Xue, Q. Fan, Y. Song, J. S. Francisco, X. C. Zeng, J. Wang, *Nature communications* **2017**, 8, 15154.

[10] a)Z. He, K. Liu, J. Wang, *Accounts of chemical research* **2018**, 51, 1082; b)K. A. Jungare, R. Radha, D. Sreekanth, *Materials Today: Proceedings* **2022**, 51, 1637; c)X. Sun, Y. Wu, Z. Song, X. Chen, *Bioactive Carbohydrates and Dietary Fibre* **2022**, 27, 100291.

[11] a)D. Wang, S. Maharjan, X. Kuang, Z. X. Wang, L. S. Mille, M. Tao, P. Yu, X. Cao, L. M. Lian, L. Lv, J. J. He, G. S. Tang, H. Yuk, C. K. Ozaki, X. H. Zhao, Y. S. Zhang, *Science*

Advances **2022**, 8, eabq6900; b)J. Z. Wu, G. Li, T. J. Ye, G. H. Lu, R. M. Li, L. F. Deng, L. Wang, M. Cai, W. G. Cui, *Chemical Engineering Journal* **2020**, 393, 124715.

[12] H. Kim, B. Kang, X. Cui, S. H. Lee, K. Lee, D. W. Cho, W. Hwang, T. B. Woodfield, K. S. Lim, J. Jang, *Advanced Functional Materials* **2021**, 31, 2011252.